

# Ultrafast, high resolution spatiotemporal mapping of energy transport dynamics for determination of energy transport properties in silicon

Mauricio Segovia and Xianfan Xu<sup>\*</sup>

*School of Mechanical Engineering and Birck Nanotechnology Center, Purdue University, West Lafayette, Indiana 47907, USA*



(Received 3 May 2023; revised 5 July 2023; accepted 30 August 2023; published 14 September 2023)

The spatiotemporal dynamics of energy carriers in silicon is studied under ultrafast laser excitation. A subpicosecond temporal resolution and precise, 10 nm spatial resolution system is used to study the spatiotemporal optical response of silicon. Two distinct sets of temporal information from a single experiment are obtained: the evolution of the peak amplitude and the spatial width of the optical reflectance trace. A modified two-temperature energy transport model incorporating the changes of carrier density under ultrafast laser excitation is used to describe the underlying carrier relaxation, carrier-phonon interaction, and energy diffusion process, and is integrated into an optical model to extract fundamental energy transport dynamics and properties. By tracking the evolution of the peak amplitude change and the spatial width with the high accuracy spatiotemporal pump probe system, the underlying relaxation rates and diffusion coefficients can be simultaneously determined. In this work, the ambipolar diffusion coefficient and the carrier-phonon scattering rate coefficient of silicon are found to be  $7.3 \text{ cm}^2 \text{ s}^{-1}$  and  $3 \times 10^{11} \text{ s}^{-1} \text{ K}^{-1}$ , respectively. Additionally, an ambipolar Auger recombination coefficient in the range of  $10^{-31} - 10^{-30} \text{ cm}^6 \text{ s}^{-1}$  is obtained. This method will be useful to determine transport dynamics and properties in many newly developed semiconductor materials.

DOI: [10.1103/PhysRevB.108.125202](https://doi.org/10.1103/PhysRevB.108.125202)

## I. INTRODUCTION

Understanding transport properties of materials necessitates a knowledge of the underlying dynamics of energy carriers. Experimentally, ultrafast pump-probe spectroscopy offers subpicosecond temporal resolution, allowing one to probe the dynamics of energy carriers in metals, semiconductors, and newly developed materials such as two-dimensional (2D) materials [1–9]. To extract transport information of energy carriers from experiments, appropriate physical models that can describe the results well are needed. Unlike metals where the energy transport dynamics after ultrafast laser excitation can be well described by a two-temperature model [10–12], ultrafast carrier dynamics in semiconductors requires additional description about the photoexcited carrier density changes and the resulting changes in its optical properties. Modifications to the two-temperature models incorporated the photoexcitation of the energy carrier to the governing energy transport equations, allowing for successful implementation and interpretation of ultrafast pump-probe experiments [13–19].

While the ultrafast measurements provide rich information, it is not immediately evident that one could simultaneously ascertain relaxation rates and diffusion coefficients from typical pump-probe experiments. To this end, an ultrafast spatiotemporal pump-probe system with subpicosecond temporal and nanometric spatial resolution is developed and used to probe both time and spatial domains simultaneously. To illustrate the processes contained in the spatial aspect of such measure-

ments, consider the spatiotemporal evolution of a continuous, conserved variable  $u$  with a characteristic relaxation rate  $\Gamma$  and time-dependent diffusivity  $D(t)$ , subject to a point source  $S$ . Its evolution in an infinite domain is governed by Eq. (1a) whose three-dimensional solution is given by Eq. (1b):

$$\frac{\partial u}{\partial t} + \nabla \cdot [-D(t)\nabla u] = -\Gamma u + S, \quad (1a)$$

$$u = C \frac{\exp[-\Gamma t]}{\sigma^3(t)} \exp\left[-4 \log 2 \frac{(x^2 + y^2 + z^2)^2}{\sigma^2(t)}\right]. \quad (1b)$$

Here,  $C$  is a constant and  $\sigma^2(t) = 16 \log 2 \int_0^t D(s) ds$  denotes a time-dependent squared full width at half maximum (FWHM<sup>2</sup>). Although the peak amplitude of  $u$  depends on both  $\Gamma$  and  $\sigma(t)$ , the spatial distribution depends solely on  $\sigma(t)$  and, therefore, on  $D(t)$ . In this work, the physical models used are more complex than Eq. (1a); however, the governing transport equations do follow a form similar to Eq. (1a), motivating the simultaneous measurements of both the peak amplitude and spatial width of an observable to extract fundamental properties such as relaxation rates and diffusion coefficients. In the measurement conducted in this work,  $u$  is the observable which is related to the reflectance of the surface of silicon to an ultrafast laser probe. Using well-established transport models for the carrier density, carrier energy, and phonon energy along with a Drude-like optical response model, relaxation times and diffusion coefficients of carriers in silicon are determined and the extracted values are shown to be well within literature values. The method developed in this work will be useful to determine transport dynamics and properties in many newly developed semiconductor materials.

<sup>\*</sup>xxu@ecn.purdue.edu

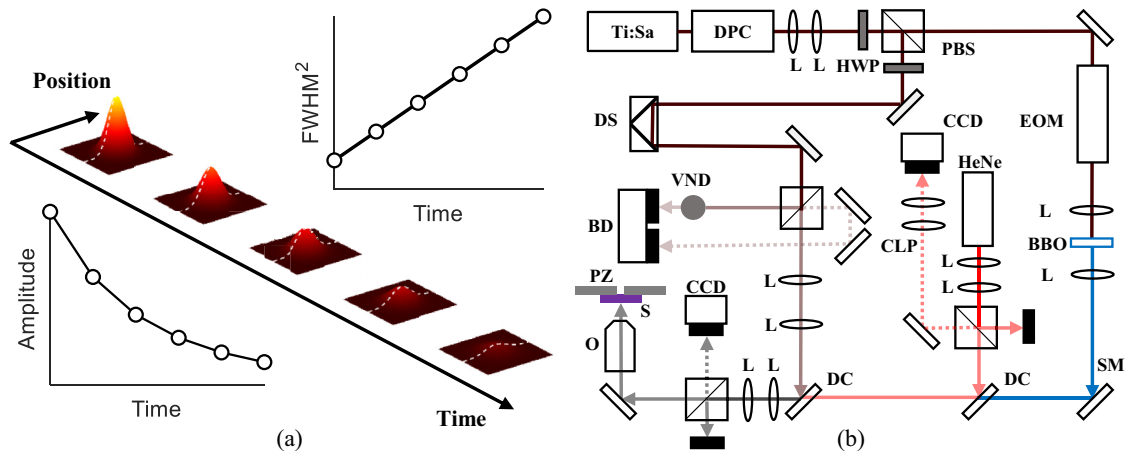


FIG. 1. (a) Depiction of the spatiotemporal measurement of the resulting optical response to an ultrafast pump laser. Here, the pump induces changes in the optical properties of the material. The probe then samples the state of the material temporally and spatially. Two distinct sets of information can be extracted: the peak amplitude (Amp.) changes and the spatial width squared (denoted as a full width at half maximum:  $\text{FWHM}^2$ ) as a function of time. (b) Schematic of the experiment. Titanium sapphire ultrafast laser (Ti:Sa), double prism compressor (DPC), lens (L), half-wave plate (HWP), polarizing beam splitter (PBS), delay stage (DS), variable neutral density filter (VND), balance detector (BD), dichroic mirror (DC), charged coupled device (CCD), cylindrical lens pair (CLP), helium neon laser (HeNe), electro-optical modulator (EOM), barium borate crystal (BBO), piezo actuated tip-tilt scanning mirror (SM), objective lens (O), sample (S), piezo stage (PZ).

## II. EXPERIMENT

Figure 1 illustrates typical ultrafast spatiotemporal measurement results along with a schematic of the experimental setup. As seen in Fig. 1(a), the evolution of the surface reflectance profile contains two parameters that one can track: the peak amplitude and spatial width. To accomplish the measurement, the output of a Ti:sapphire, 80 MHz femtosecond laser with 1.55 eV center photon energy is split into a pump arm and a probe arm. The pump arm is modulated by an electro-optical modulator and then frequency doubled to 3.1 eV center photon energy. The time delay between the pump and probe is controlled by a mechanical delay stage installed along the probe arm path. The pump is steered to the shared optical path using a piezo actuated tip-tilt mirror. Lastly, the reflectance change of the probe arm is measured by a balance detector and a lock-in amplifier.

Due to chromatic aberration, the pump and probe beam waists do not meet at the same point along the optical axis when both enter an objective collimated. Tunable divergences are implemented with lens pairs resulting in beam waist overlap with 550 nm FWHM sizes measured by the knife edge method. Pulse durations measured by autocorrelation are around  $\sim 500$  fs FWHM, establishing the subpicosecond resolution of the experimental setup. The tip-tilt mirror actuated displacement of the pump relative to the probe has a resolution of 2 nm at the surface of the sample which is quantified by monitoring the movement of the pump at the probe beam waist location by successive knife edge measurements; this establishes the lower limit of the uncertainty to all spatial measurements. It is the positioning accuracy of this mirror that allows for the nanometric displacement resolution of the pump relative to the probe at the sample surface. A consistent working distance is maintained using a home built autofocus system as depicted in Fig. 1(b). Additional details of this system can be found in previous works [20]. The accuracy of

the actual spatial measurement will be discussed together with the experimental results in the next section.

## III. EXPERIMENTAL RESULTS

In the experiment, a piece of silicon ([111] *n* type, 50–80  $\Omega$  cm,  $\sim 500$   $\mu\text{m}$  thickness from Siltronic AG) is mounted on a piezo stage whose positioning is used for all spatial measurement calibrations stated before. Using an incident pump power of 2 mW and incident probe power of 0.02 mW, the change in the reflected probe power is monitored as a function of the temporal delay and spatial displacement between the pump and probe. The acquired reflectance trace allows for the location of the temporal and spatial location of maximum pump-probe overlap based on the maximum reflectance change. With the location of maximum overlap determined, the pump is displaced relative to the probe with precise nanometric steps for a given temporal delay. The dataset presented in Fig. 2 shows the experimental data along with the best fitted simulated reflectance amplitude and spatial width. Figure 2(a) illustrates a spatiotemporal measurement performed by scanning the pump along a one-dimensional (1D) spatial axis in the in-plane direction relative to the silicon surface. It is found that the dataset is radially symmetric. The experimental dataset is numerically deconvolved by considering the functional form of the Gaussian intensity distribution of the probe, effectively reducing the measured spatial  $\text{FWHM}^2$  by subtracting its value by the  $\text{FWHM}^2$  of the probe intensity distribution. Representative 1D spatial cut lines of Fig. 2(a) are presented in Fig. 2(b). The peak amplitude corresponds to the maximum of each 1D cut line at a given delay time whereas the width corresponds to the FWHM of each cut line at a given delay time.

Figures 2(c) and 2(d) show the simulated reflectance trace of the amplitude and spatial width, respectively, and are in good agreement with the dataset. The parameters used for

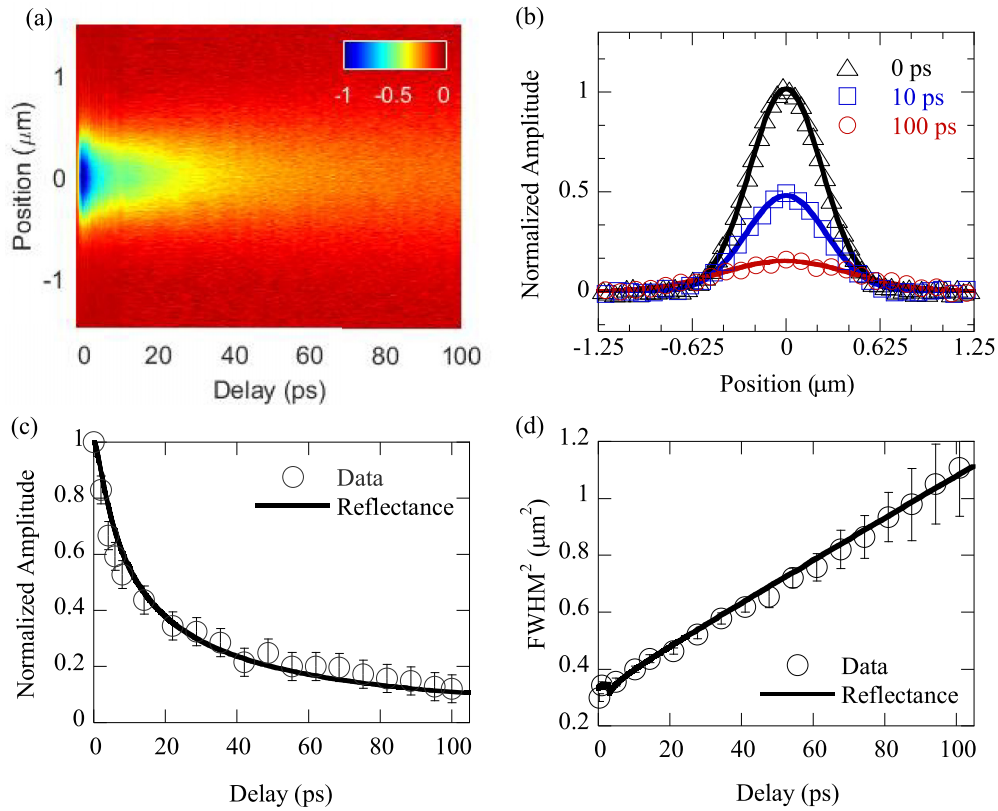


FIG. 2. (a) Color map of a spatiotemporal measurement on silicon. (b) Representative spatial 1D cut lines of (a) at three different delay times. (c) Extracted peak amplitude changes at position  $0 \mu\text{m}$  as a function of delay time along with the best fitted simulated result. (d) A plot of the extracted  $\text{FWHM}^2$  as a function of delay time along with the best fitted simulated result. The error bars on the data points denote the measurement uncertainty and their calculation is described in the main text.

Figs. 2(c) and 2(d) are the best fitted parameters listed in Table I, along with the nominal values from the literature, and will be discussed later. Here, we will first discuss the measurement uncertainties as they are critical for determining the physical parameters of interest. Figure 2(c) shows the decay of the amplitude of reflectivity when the probe beam is located at the center of the pump by drawing a 1D temporal cut line about position  $0 \mu\text{m}$  in Fig. 2(a), similar to a traditional pump-probe measurement consisting of spatially overlapped beams. The measurement uncertainty for the amplitude is calculated by first sampling the lock-in amplifier output at long delay times and creating a histogram when the pump-probe signal is at its weakest; two standard deviations of this histogram define the uncertainty. This corresponds to a maximum amplitude uncertainty of 5% relative to the lock-in value denoting the maximum reflectance change for the dataset presented in Fig. 2(c). Second, the spatial width of the reflectance trace is plotted by measuring the FWHM of a

1D spatial cut line about any delay time; three representative examples are shown in Fig. 2(b). The FWHM for each delay time is plotted in Fig. 2(d), presented as a  $\text{FWHM}^2$ . The measurement uncertainty for the  $\text{FWHM}^2$  is calculated by first extracting a 1D cut line about a given time delay. The amplitude uncertainty is known. The uncertainty in the position coordinate is taken as the displacement resolution of  $2 \text{ nm}$ . A Monte Carlo approach is then used to simulate 10 000 possible 1D spatial cut lines for a given delay time by assigning a uniform probability distribution to the position uncertainty and a normal probability distribution to the amplitude uncertainty; a histogram of the best fitted FWHM values is then produced. The uncertainty in the measured FWHM is then defined as two standard deviations of this histogram. It should be noted that as the signal strength weakens at longer delay times, the uncertainty in the measured FWHM increases. Here, the minimum measurement uncertainty of 2% ( $0.01 \mu\text{m}$  for a FWHM value of  $0.55 \mu\text{m}$ ) occurs at  $0 \text{ ps}$  delay time (when the signal

TABLE I. Fitting and normal values of parameters of interest.

	$D_o \text{ (cm}^2 \text{ s}^{-1}\text{)}$	$(BT_o)^{-1} \text{ (fs)}$	$\gamma_3 \text{ (} 10^{-31} \text{ cm}^6 \text{ s}^{-1}\text{)}$	$k_p \text{ (W m}^{-1} \text{ K}^{-1}\text{)}$	$k_n \text{ (W m}^{-1} \text{ K}^{-1}\text{)}$
Nominal	20 <sup>a</sup>	30 <sup>b</sup>	2 <sup>c</sup>	150 <sup>d</sup>	$\ll 1$ <sup>d</sup>
Best fitted	7.3	$> 15$	1–10	n/a	n/a

<sup>a</sup>Reference [21]; <sup>b</sup>Ref. [22]; <sup>c</sup>Ref. [23]; <sup>d</sup>Ref. [24].

is the strongest) and the maximum measurement uncertainty of 10% (0.10  $\mu\text{m}$  for a FWHM of 1.00  $\mu\text{m}$ ) occurs at 100 ps delay time (when the signal is the weakest). The conversion to an uncertainty in a measured FWHM<sup>2</sup> is then readily found. Additional details of the procedure for quantifying the measurement uncertainty can be found in previous works [15].

#### IV. THEORETICAL MODELS

The spatiotemporal measurement used in this work is inherently a measurement of the optical response of the excited material. As silicon is an indirect band gap semiconductor, the measured dynamics of photoexcited carriers will depend on both the pump and probe photon energies. In this work, carriers are excited by a 3.1 eV pump, well above the 1.2 eV indirect band gap of silicon at room temperature and slightly below the 3.3 eV direct transition at the zone center in reciprocal lattice space [25,26]. For complete promotion to the conduction band of silicon, indirect transitions necessitate mediation by the underlying phonon system. However, it has been shown that due to thermal broadening of absorption at room temperature and the strong photonic field generated by the pump, direct transitions can occur at 3.1 eV, resulting in the formation of electron-hole pairs without the aid of the phonon system [26,27]. In the model presented below, a given photon of energy  $\hbar\omega$  will be absorbed by an electron such that  $\hbar\omega = E_g + KE$  where  $E_g$  is the indirect band gap of silicon and  $KE$  is the excess kinetic energy of the electron which will be discussed shortly.

The initial evolution of the system will be driven by the changes in carrier density. The timescales considered in this work allow a continuum approach to be taken for the transport variables of interest: carrier density, carrier energy, and phonon energy. Beginning with the works of van Driel [13], and expanded upon by others [14,17–19,28], the spatiotemporal evolutions of the transport variables in this work are modeled as

$$\frac{\partial n}{\partial t} + \nabla \cdot \vec{J}_n = S_n, \quad (2a)$$

$$\frac{\partial U_n}{\partial t} + \nabla \cdot \vec{J}_U = S_U, \quad (2b)$$

$$\frac{\partial U_p}{\partial t} + \nabla \cdot \vec{J}_p = S_p, \quad (2c)$$

where  $n$  is the carrier density,  $U_n$  is the carrier energy, and  $U_p$  is the phonon energy. The total internal energy of the carrier system is defined as  $U_n = nE_g + 3nk_B T_n$  with contributions from the excess kinetic energy of carriers where  $E_g$  is the indirect band gap of silicon,  $k_B$  is Boltzmann's constant, and  $T_n$  is the effective carrier temperature. For the phonon system,  $U_p = C_p T_p$  where  $C_p$  is the phonon volumetric heat capacity and  $T_p$  is the effective phonon temperature. The flux of each transport variable is represented as  $\vec{J}$  and defined as [14,17–19,28]

$$\vec{J}_n = -D_n \left( \nabla n + \frac{n}{2T_n} \nabla T_n \right), \quad (3a)$$

$$\vec{J}_U = (E_g + 4k_B T_e) \vec{J}_n - k_n \nabla T_n, \quad (3b)$$

$$\vec{J}_p = -k_p \nabla T_p, \quad (3c)$$

where  $D_n$  is the ambipolar diffusivity,  $k_n$  is the effective sum of the carrier's (electron and hole) thermal conductivity, and  $k_p$  is the phonon thermal conductivity. The dependence of  $D_n$  on  $T_p$  takes the form of  $D_n = D_o \frac{T_o}{T_p}$  where  $T_o$  is the initial temperature of the entire system [13,17]. The effective carrier thermal conductivity has been shown to depend on both the carrier temperature and density, achieving a maximum value of around  $\sim 1 \text{ W m}^{-1} \text{ K}^{-1}$  with the maximum temperature and carrier density achieved in the measurement [29,30]. However, the energy of the carrier system rapidly relaxes within  $\sim 1$  ps (see next section) and, therefore, the effective thermal conductivity takes on a constant value of  $0.01 \text{ W m}^{-1} \text{ K}^{-1}$ . Since the simulated phonon temperature does not rise more than 10% of the initial temperature, the thermal properties of the phonon system are taken as constant with a thermal conductivity and volumetric heat capacity of  $149.09 \text{ W m}^{-1} \text{ K}^{-1}$  and  $1.6 \text{ MJ m}^{-3} \text{ K}^{-1}$ , respectively. The effect of variations of thermal conductivity from these constants will be discussed later.

The source/sink terms for the respective transport variable are represented as  $S$  and are defined as [14,17–19,28]

$$S_n = \frac{\alpha I}{\hbar\omega} + \delta n - \gamma_1 n - \gamma_2 n^2 - \gamma_3 n^3, \quad (4a)$$

$$S_U = \alpha I - G_o n (T_n - T_p), \quad (4b)$$

$$S_p = G_o n (T_n - T_p), \quad (4c)$$

where  $\alpha$  is the inverse of the optical penetration depth,  $I$  is the incident laser radiation after reflection,  $\omega$  is the pump angular frequency,  $\hbar$  is the reduced Planck's constant,  $\delta$  is the impact ionization coefficient,  $\gamma_1$  denotes a first order recombination rate,  $\gamma_2$  denotes a second order recombination rate coefficient, and  $\gamma_3$  is the ambipolar Auger recombination coefficient. The use of first and second order recombination is omitted due to the low probability of it occurring in indirect band gap materials, i.e.,  $\gamma_1 = 0 \text{ s}^{-1}$  and  $\gamma_2 = 0 \text{ s}^{-1} \text{ m}^3$ . Previous works have shown that this mechanism is important only at high laser intensities which are an order of magnitude higher than the ones used in this work [31]. Auger recombination is included due to the large number of excess carriers generated during laser excitation. The carrier-phonon coupling constant per carrier density is defined as  $G_o = \frac{B\pi^2 m_e v_s^2}{6}$  where  $B$  is a carrier-optical phonon scattering rate coefficient used in the optical model [Eq. (5)],  $m_e$  is the effective carrier mass, and  $v_s$  is the speed of sound in the material [18,32,33]. A representative simulation output of the peak values of the carrier temperature, phonon temperature, and carrier density with the incident pump power of 2 mW is shown in Figs. 3(a) and 3(b) to illustrate their temporal variations and typical values.

Throughout the relaxation process, the optical response, encoded in the dielectric constant, changes as well. Typically, a Drude model is applied to analyze the optical response of photoexcited carriers to an ultrafast probe laser [17,19,34,35].

$$\epsilon = \epsilon_\infty + \Delta\epsilon_{\text{bsf}} + \Delta\epsilon_{\text{bsr}} - \frac{\omega_p^2}{\omega^2 (1 + i\frac{\Gamma}{\omega})}. \quad (5)$$

Here,  $\epsilon_\infty$  is the high frequency electric permittivity,  $\omega$  is the frequency of the probe,  $\omega_p^2 = \frac{e^2 n}{\epsilon_o m_e}$  is the plasma frequency where  $e$  is the electron charge,  $\epsilon_o$  is the vacuum electric



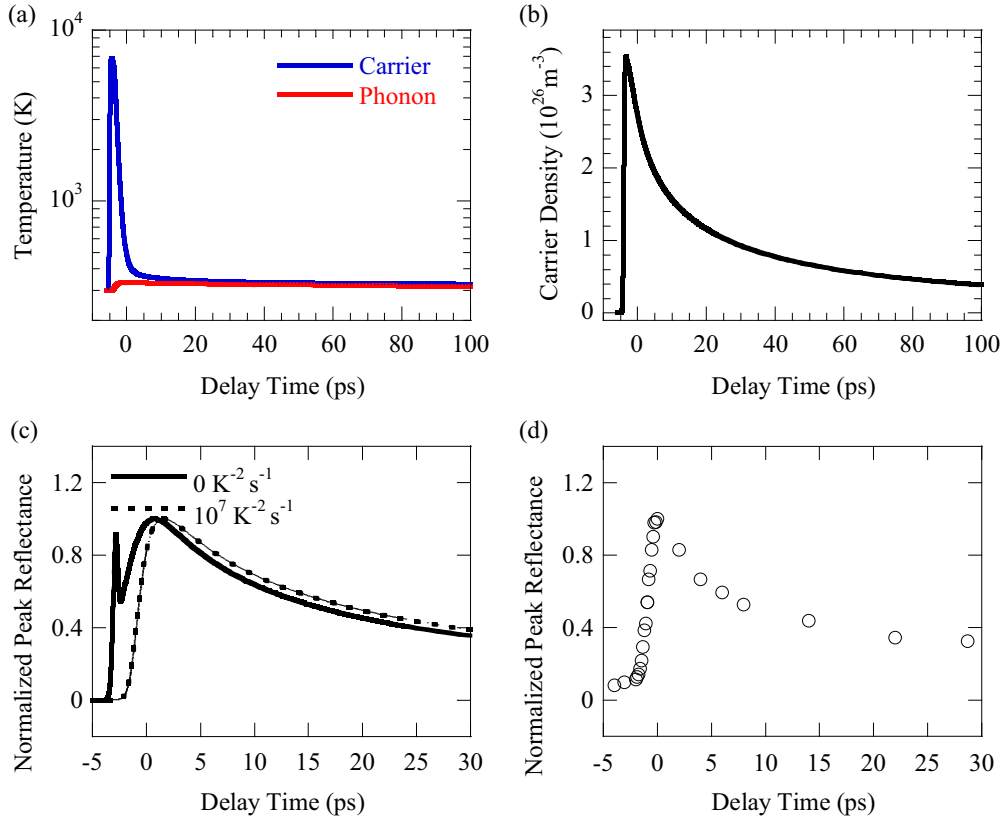


FIG. 3. (a) Peak temperature evolution of the carrier (blue) and phonon (red) systems. The difference in temperature quickly decreases within the first few picoseconds. (b) The peak carrier density evolution as a function of time. Here, the carrier density remains on the same order of magnitude throughout the experimentally probed delay times. (c) From simulation, the omission of carrier-carrier scattering results in a reflectance curve (solid) that contains prezero delay features that are not contained in the raw data (d). However, applying carrier-carrier scattering (dashed) shows greater fidelity to the experimental data.

permittivity, and  $\Gamma$  is an effective scattering rate. State-band renormalization ( $\Delta\epsilon_{\text{sb}}^{\text{r}}$ ) is dominant when the excited carrier density is near the initial, unexcited valence band population [34] ( $\sim 10^{23} \text{ cm}^{-3}$  for silicon [36]). As shown in the following discussion, the excited carrier density is more than three orders of magnitude less than this value and thus SBF is deemed negligible. Band structure renormalization explicitly depends on the evolution of the band structure due to changes in the occupation of the valence and conduction bands as well as changes in the overall temperature of the system [34,37]. Experiments show that the dynamics of renormalization due to transient changes in occupation in other materials occurs on the order of hundreds of femtoseconds which is faster than what can be resolved in our experiments [38,39]. For the purposes of analyzing relaxation rates inherent to the transport variables of interest after a few picoseconds, this effect is not included. In this work, carrier-carrier, electron-hole, and carrier-phonon scattering rates are used and read as [17,18,33]

$$\Gamma_{\text{cc}} = AT_n^2, \quad (6a)$$

$$\Gamma_{\text{eh}} = \sqrt{\frac{3}{2m_e}} \frac{\pi\epsilon_0}{e^2} (k_B T_n)^{\frac{3}{2}}, \quad (6b)$$

$$\Gamma_{\text{cp}} = BT_p, \quad (6c)$$

where  $A$  is a coefficient that is assumed to be similar to that of gold of  $10^7 \text{ s}^{-1} \text{ K}^{-2}$  [40], and  $\Gamma = \Gamma_{\text{cc}} + \Gamma_{\text{eh}} + \Gamma_{\text{cp}}$ . It should be noted that carrier-carrier scattering (between particles of the same sign) conserves momentum, and therefore, usually does not contribute to the effective scattering rate [41]. However, it has been shown that carrier-carrier scattering can contribute to scattering rates in silicon due to its band structure [42]. Here, the temperature dependence of the carrier-carrier scattering rate is modeled similar to gold in Eq. (6a). As for the temperature dependence of the electron-hole scattering rate, theoretical [43] and experimental [44] works have shown that if the temperature of the carrier system is above the Fermi temperature, then electron-hole scattering rates tend to decrease with temperature. In our work, the simulated carrier temperature reaches a maximum value of 6000 K, then quickly falls to near thermal equilibrium with the phonon system, at about 330 K or less. The estimated Fermi temperature for the simulated carrier density is around 5000 K. Below the Fermi temperature, the electron-hole scattering rate can be modeled as increasing with increasing temperature [43,44]. In our work, the modeling used in [17] is incorporated into Eq. (6b). It should be noted that omission of Eq. (6a) in simulation shows different features before the peak normalized reflectance value is reached that do not agree with the acquired data as seen in Figs. 3(c) and 3(d). However, the inclusion or omission of Eq. (6a) does not affect the

determination of the parameters as experimental detection of the differences in simulation is beyond the current resolution of the system. Nevertheless, Eq. (6a) is included for completeness.

Equation (5) is computed as a function of all transport variables. Because the experimental data are found to be radially symmetric, the simulation domain is made to be axisymmetric for computational efficiency. The boundary condition at the irradiated surface is taken as zero flux and all other dimensions are taken as semi-infinite. Computationally, it is found that a radial dimension of  $10\text{ }\mu\text{m}$  and an axial dimension of  $10\text{ }\mu\text{m}$ , far larger than the optical penetration depth and beam waist, were sufficient for numerical convergence as well as run time. The reflectance at the irradiated surface is calculated using Fresnel's equations. The resulting reflectance map at the surface of the silicon is then compared with the numerically deconvolved experimental dataset.

## V. RESULTS AND DISCUSSIONS

Of great importance to this work is assessing the ability of the high accuracy spatiotemporal measurement in determining multiple physical parameters from a single experiment. To this end, a numerical analysis is conducted on the acquired data. First, the collected  $\text{FWHM}^2$  data are analyzed by fitting a line to Fig. 2(d), resulting in a slope of  $D_{\text{ex}} = 81\text{ cm}^2\text{ s}^{-1}$  with a y intercept of  $0.32\text{ }\mu\text{m}^2$  (corresponding to an initial spatial width of  $\sim 550\text{ nm}$ , i.e., the beam waist of the pump). From Eq. (1b), the slope of the  $\text{FWHM}^2$  can be immediately related to a diffusion coefficient,  $D$ , by  $D_{\text{ex}} = 16 \log 2D$  resulting in an experimental diffusion coefficient of  $D = 7.3\text{ cm}^2\text{ s}^{-1}$ . Silicon is reported to have a nominal ambipolar diffusivity [45] of  $\sim 20\text{ cm}^2\text{ s}^{-1}$ . Due to the timescales studied in this work, the main driver of diffusion is the carrier system, effectively dictating the evolution of the  $\text{FWHM}^2$  at early delay times. The value obtained from the slope of Fig. 2(d), however, differs from the nominal value. This may be due to the number of photoexcited carriers generated during the ultrafast pump excitation. One can make a conservative estimate for the photoexcited carrier density by considering the total energy deposited within the optical penetration depth ( $\sim 100\text{ nm}$  at  $3.1\text{ eV}$  [25]),  $d$ , by the pump of photon energy,  $\hbar\omega$ , as  $\Delta n \approx \frac{1}{d} \frac{F}{\hbar\omega}$  where  $F$  is the absorbed fluence. Here,  $\Delta n \approx 2 \times 10^{20}\text{ cm}^{-3}$ , above the expected initial carrier density of around  $10^{14}\text{ cm}^{-3}$  at room temperature. Within the 100 ps of observation, the simulated excess carrier density only drops one order of magnitude; therefore, the measured ambipolar diffusivity is for a carrier density of that order. It has been shown that an increase in carrier density and temperature will cause a reduction in the mobility of electrons and holes, in effect reducing the ambipolar diffusion coefficient anywhere from 18 to  $2.5\text{ cm}^2\text{ s}^{-1}$  at carrier densities on the same order as those in this work [21,46,47]. A previous measurement [47] at high photoexcited carrier densities yielded an ambipolar diffusion coefficient as low as  $2.5\text{ cm}^2\text{ s}^{-1}$ . However, the analysis conducted in [47] was done at the nanosecond timescale and with different photon energies, and the result may have been heavily influenced by the phonon system driving the optical response. Here, the carrier system relaxes within a characteristic electron-hole recombination time as low as  $\sim 1\text{ ns}$  [23,48],

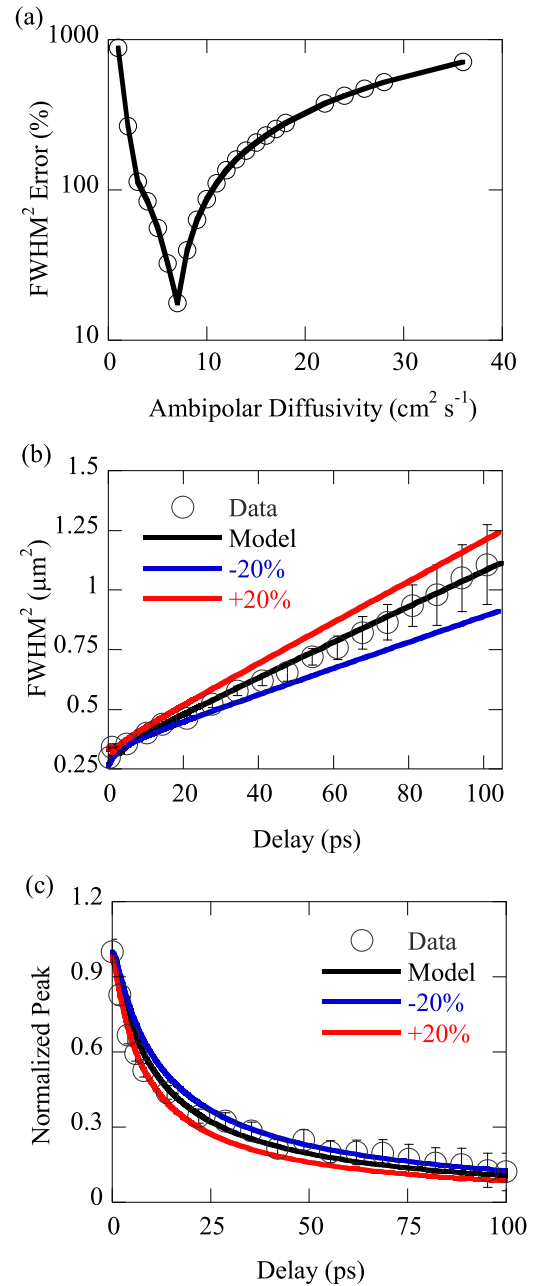


FIG. 4. Numerical analysis of the sensitivity of the model to the ambipolar diffusion coefficient. (a)  $\text{FWHM}^2$  error relative to the maximum measurement uncertainty of 100 nm. Due to the high accuracy of the spatial measurement, an excellent fit is accomplished at  $7\text{ cm}^2\text{ s}^{-1}$ . (b) Illustration of the variation of the  $\text{FWHM}^2$  to a  $\pm 20\%$  variation in the ambipolar diffusivity. The effects on the peak amplitude are shown in (c). Within the measurement uncertainty, it is clear that the  $\text{FWHM}^2$  is more sensitive than the peak amplitude in determining the ambipolar diffusion coefficient.

allowing the thermal system of the carriers to drive energy diffusion and dictate the overall optical response. Another important detail to note is that depending on the photon energy used to excite the carrier, the effective estimated diffusivity may be different [49]. A lower limit of  $\sim 4.5\text{ cm}^2\text{ s}^{-1}$  was estimated for electrons excited with photon energies similar

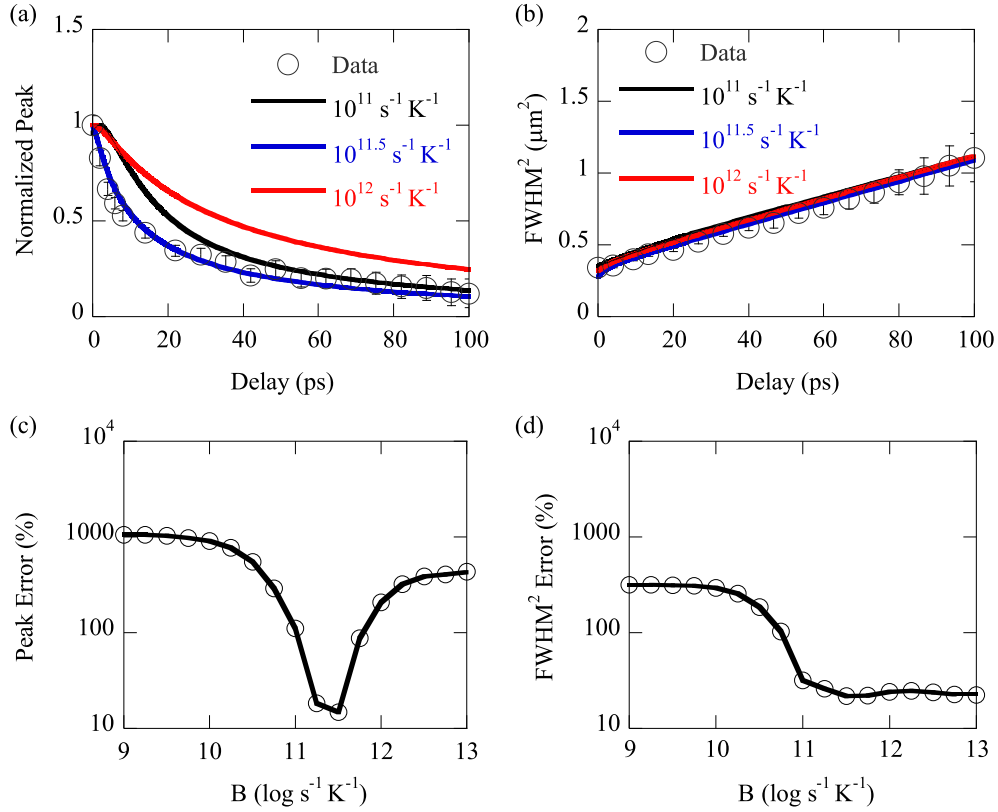


FIG. 5. Numerical analysis of the sensitivity of evolution of the peak amplitude (a) and spatial  $\text{FWHM}^2$  (b) as a function of the carrier-phonon scattering rate. There is a clear minimum identified for the peak amplitude in (c), yet not identified for the  $\text{FWHM}^2$  in (d). This suggests that the carrier-phonon energy relaxation rate mainly dictates the evolution of the peak amplitude, and therefore, can be inferred from (a), (c).

to the pump used in this work; this value agrees better with the result obtained in this work.

Figure 4(a) shows a numerical analysis for determining the ambipolar diffusion coefficient, computing the spatiotemporal evolution of the reflectance to different modeled ambipolar diffusion coefficients and comparing the results to the acquired data. The error is calculated as a percentage relative to the maximum measurement uncertainty in the  $\text{FWHM}^2$  of  $0.10 \mu\text{m}^2$ . A clear minimum is achieved at  $7 \text{ cm}^2 \text{ s}^{-1}$ . Figure 4(b) illustrates the variation of the model output to

a  $\pm 20\%$  variation to the ambipolar diffusivity. Clearly, this variation is well within the measurement uncertainty. The peak amplitude versus time is also influenced by the variation of ambipolar diffusivity; however, the same variation produces changes that are smaller, close to the measurement uncertainty. Therefore, the  $\text{FWHM}^2$  is more sensitive to the ambipolar diffusion coefficient. This result is expected from a mathematical standpoint from observing Eqs. (1a) and (1b) since transient diffusion processes have spatial widths that are highly dependent on their diffusion coefficients.

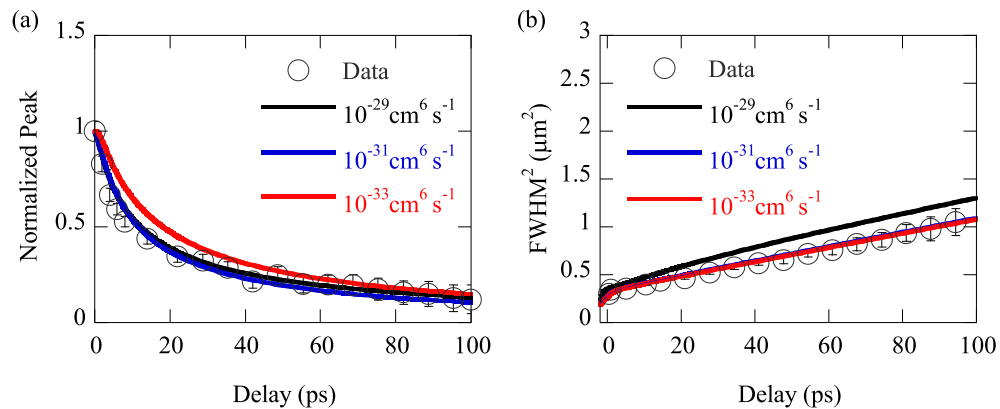


FIG. 6. Variation of simulated peak amplitude as a function of the (a) Auger recombination coefficient  $\gamma_3$ . Variation of the  $\text{FWHM}^2$  as a function of the (b) Auger recombination coefficient

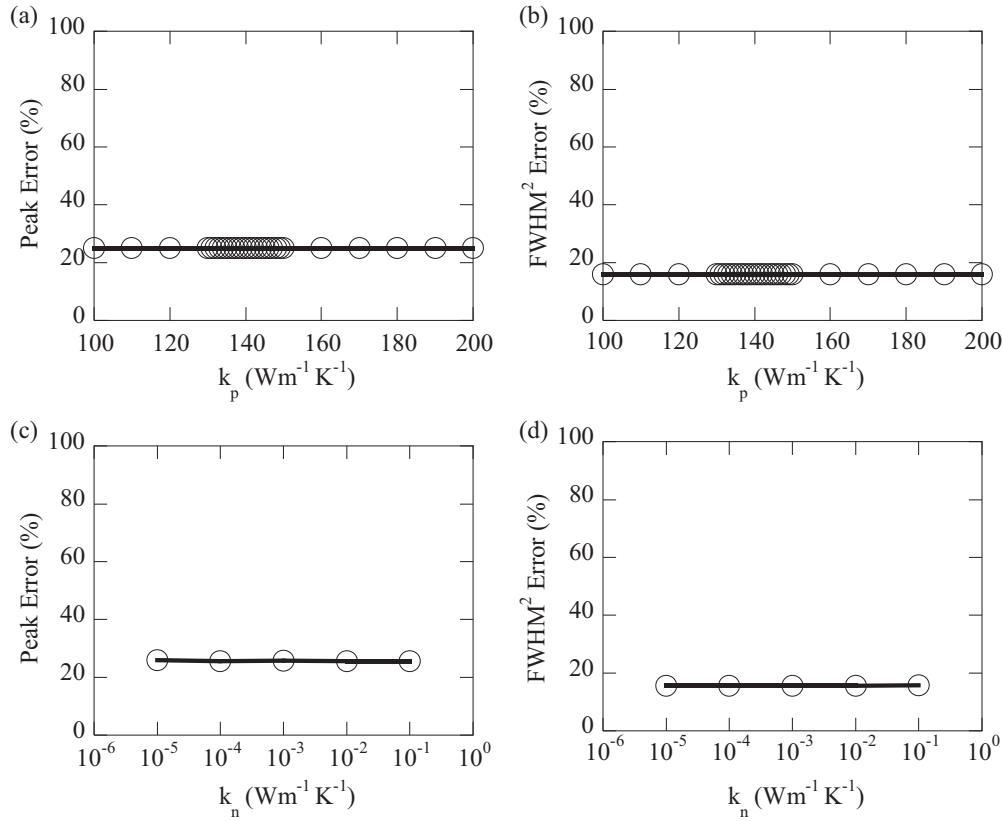


FIG. 7. Numerical analysis of the sensitivity of evolution of the peak amplitude (a) and spatial FWHM<sup>2</sup> (b) as a function of the phonon thermal conductivity  $k_p$  for a fixed electron thermal conductivity  $k_n$  of  $1.0 \text{ W m}^{-1} \text{ K}^{-1}$ . By fixing the total value of the thermal conductivity of silicon, the sensitivity of the peak amplitude (c) and spatial FWHM<sup>2</sup> (d) on the carrier thermal conductivity  $k_n$  is shown. At the timescales analyzed in this work, there is a lack of sensitivity of optical response to thermal transport.

The carrier relaxation rates can also be analyzed from the measurement. Encoded in the optical response is the dependency of carrier-optical phonon scattering rate temperature coefficient  $B$  as seen in Eq. (6c). This dependency directly influences the overall carrier-phonon energy coupling seen in Eqs. (4b) and (4c) through the carrier-phonon energy coupling term,  $G_{on}$ . Since a Drude model is invoked in determining the optical response, the characteristic scattering rates are those of the carrier's momentum. Theoretical works have used this momentum scattering rate to then define the overall energy coupling strength between carriers in phonons [32,33,50]. By defining a carrier-phonon energy coupling constant, one can then define an effective energy coupling rate through either Eq. (2b) or (2c) as will be seen below.

The parameter  $B$  is varied in simulation and the resulting best fitted value and sensitivity are presented in Fig. 5. The best fitted value of  $B$  occurs at  $\sim 10^{11.5} \text{ K}^{-1} \text{ s}^{-1}$ , which corresponds to a room temperature carrier-optical phonon scattering time of  $\sim 10 \text{ fs}$  as defined in the Drude model. The value of  $10 \text{ fs}$  is on the same order as other works where the dynamics of an electron with excitation energy of  $3.1 \text{ eV}$  was studied [37] as well as the typical lifetime of optical phonons in silicon [22,51], and on the same order as first principle calculations [52]. Variations to  $B$  show that the peak amplitude fits well to a unique value of  $B$  whereas the FWHM<sup>2</sup> appears to be well fitted up to a lower limit as seen

in Figs. 5(a) and 5(b), respectively. Notably, the amplitude data show a clear minimum in its error whereas the FWHM<sup>2</sup> only shows a range in which the error reaches a lower limit as seen in Figs. 5(c) and 5(d). With this in consideration, the value of  $B$  extracted from the transport model directly influences the energy scattering rate through the definition of the carrier-phonon coupling constant  $G_o$  described previously. An effective energy coupling time between the carrier and phonon system can then be found through Eqs. (2b) and (4b) as  $\tau_E = \frac{3k_B}{G_o} \approx 1.5 \text{ ps}$ .

A discussion on the range of timescales presented is now warranted. The experiment spans 1–100 ps in delay time. As noted in Fig. 5(a), the carrier-optical phonon scattering temperature coefficient, defined in Eq. (6c), heavily influences the reflectance profile since the phonon temperature system is undergoing transient changes throughout the entire procedure. Therefore, due to both the experimental accuracy and model sensitivity, the coefficient  $B$  can be extracted. This coefficient is then used to directly define the carrier-optical phonon scattering time through Eq. (6c), giving the smallest extracted time constant of  $\approx 10 \text{ fs}$ . Additionally, through the definition of the carrier-phonon energy coupling constant in Eq. (4b), the scattering time directly influences the energy coupling time (defined as the characteristic decay time of the temperature difference between the carrier and phonon temperature), giving a value of  $\approx 1.5 \text{ ps}$ .



Since the carrier densities studied in this work are high, Auger recombination needs to be considered. However, the typical timescales of Auger recombination, even at high carrier densities, are on the order of nanoseconds, beyond the timescales studied in this work. As an estimation of a characteristic Auger recombination time, for an excess carrier density of  $10^{20} \text{ cm}^{-3} \text{ s}^{-1}$ ,  $\frac{1}{\tau_A} \approx \gamma_3 n^2$  which comes out to  $\sim 1 \text{ ns}$  with a nominal value [23] of  $\gamma_3 = 10^{-31} \text{ cm}^6 \text{ s}^{-1}$ . For completeness, the variation of the Auger recombination parameter on the peak amplitude [Fig. 6(a)] and the FWHM<sup>2</sup> [Fig. 6(b)] is shown. It is seen that the Auger recombination coefficient is within a range of  $10^{-32} \text{ cm}^6 \text{ s}^{-1} < \gamma_3 < 10^{-30} \text{ cm}^6 \text{ s}^{-1}$ , in agreement with the literature value mentioned above. Resolving this coefficient with more sensitivity would require probing at longer delay times.

Lastly, we discuss the effect of the thermal diffusion process on the optical response. As stated before, at the timescales studied, the carrier diffusion process dominates the optical response rather than the thermal diffusion process. This can be first seen numerically by fixing the total carrier thermal conductivity to an upper theoretical value [24] of  $1 \text{ W m}^{-1} \text{ K}^{-1}$  and sweeping the phonon thermal conductivity. Figure 7 illustrates the lack of sensitivity to thermal transport at the timescales used in the experiment by computing the respective errors of the peak amplitude [Fig. 7(a)] and spatial width [Fig. 7(b)] as a function of the phonon thermal conductivity. As stated before, the electron contribution to thermal transport is heavily dependent on changes in the carrier density and carrier temperature. However, even with this dependence, the carrier temperature rise and fall is on the

order of  $\sim 1 \text{ ps}$  as shown in Fig. 3(a). Additionally, the peak of the reflectance occurs after the peak carrier temperature due to the increase in carrier density, effectively masking the effects that the carrier thermal transport properties have on the observable. Figures 7(c) and 7(d) illustrate the sensitivity to the carrier thermal conductivity by fixing the total thermal conductivity,  $k_T$ , of silicon and letting  $k_T = k_p + k_n$ . It is seen that the carrier thermal conductivity does not influence the optical measurement.

## VI. CONCLUSION

In conclusion, a high accuracy spatiotemporal pump probe system with subpicosecond resolution and nanometric spatial resolution is used to simultaneously measure the evolution of the peak amplitude and spatial width of the reflectance of silicon after ultrafast laser excitation. Applying well-established transport models for the timescales of interest, relaxation rates and diffusion coefficient are simultaneously ascertained. Variation to the transport parameters shows the FWHM<sup>2</sup> measurement is highly sensitive to the diffusion coefficients whereas the peak amplitude is highly sensitive to relaxation rates, within measurement uncertainty. This methodology can be used to directly extract transport properties from a single measurement and will be useful for the study of many newly developed semiconductor materials.

## ACKNOWLEDGMENT

The financial support from the National Science Foundation (Grant No. CBET-2051525) is gratefully acknowledged.

- 
- [1] N. Del Fatti, C. Voisin, M. Achermann, S. Tzortzakis, D. Christofilos, and F. Vallée, Nonequilibrium electron dynamics in noble metals, *Phys. Rev. B* **61**, 16956 (2000).
  - [2] C. H. Lui, K. F. Mak, J. Shan, and T. F. Heinz, Ultrafast Photoluminescence from Graphene, *Phys. Rev. Lett.* **105**, 127404 (2010).
  - [3] D. Giovanni, H. Ma, J. Chua, M. Grätzel, R. Ramesh, S. Mhaisalkar, N. Mathews, and T. C. Sum, Highly spin-polarized carrier dynamics and ultralarge photoinduced magnetization in  $\text{CH}_3\text{NH}_3\text{PbI}_3$  perovskite thin films, *Nano Lett.* **15**, 1553 (2015).
  - [4] L. Tian, L. Di Mario, V. Zannier, D. Catone, S. Colonna, P. O’Keeffe, S. Turchini, N. Zema, S. Rubini, and F. Martelli, Ultrafast carrier dynamics, band-gap renormalization, and optical properties of ZnSe nanowires, *Phys. Rev. B* **94**, 165442 (2016).
  - [5] V. Iyer, Y. P. Chen, and X. Xu, Ultrafast Surface State Spin-Carrier Dynamics in the Topological Insulator  $\text{Bi}_2\text{Te}_3$ , *Phys. Rev. Lett.* **121**, 026807 (2018).
  - [6] E. M. Van Goethem, C. W. Pinion, E. E. M. Cating, J. F. Cahoon, and J. M. Papanikolas, Observation of phonon propagation in germanium nanowires using femtosecond pump-probe microscopy, *ACS Photonics* **6**, 2213 (2019).
  - [7] M. Wörle, A. W. Holleitner, R. Kienberger, and H. Iglev, Ultrafast hot-carrier relaxation in silicon monitored by phase-resolved transient absorption spectroscopy, *Phys. Rev. B* **104**, L041201 (2021).
  - [8] Y. Lu, X. Tan, Y. Du, D. Ma, and W. Ma, Direct observation of ultrafast carrier coupling dynamics in monolayer graphene/metal system, *Int. J. Heat Mass Transfer* **197**, 123322 (2022).
  - [9] K. Birkmeier, T. Hertel, and A. Hartschuh, Probing the ultrafast dynamics of excitons in single semiconducting carbon nanotubes, *Nat. Commun.* **13**, 6290 (2022).
  - [10] S. I. Anisimov, B. L. Kapeliovich, and L. T. Perel’man, electron emission from metal surfaces exposed to ultrashort laser pulses, *Zh. Eksp. Teor. Fiz.* **66**, 776 (1974) [*Sov. Phys. JETP* **39**, 375 (1974)].
  - [11] M. Bonn, D. N. Denzler, S. Funk, M. Wolf, S.-S. Wellershoff, and J. Hohlfeld, Ultrafast electron dynamics at metal surfaces: Competition between electron-phonon coupling and hot-electron transport, *Phys. Rev. B* **61**, 1101 (2000).
  - [12] R. B. Wilson, J. P. Feser, G. T. Hohensee, and D. G. Cahill, Two-channel model for nonequilibrium thermal transport in pump-probe experiments, *Phys. Rev. B* **88**, 144305 (2013).
  - [13] H. M. van Driel, Kinetics of high-density plasmas generated in Si by 1.06- and 0.53- $\mu\text{m}$  picosecond laser pulses, *Phys. Rev. B* **35**, 8166 (1987).
  - [14] J. K. Chen, D. Y. Tzou, and J. E. Beraun, Numerical investigation of ultrashort laser damage in semiconductors, *Int. J. Heat Mass Transfer* **48**, 501 (2005).

- [15] G. D. Tsibidis, M. Barberoglou, P. A. Loukakos, E. Stratakis, and C. Fotakis, Dynamics of ripple formation on silicon surfaces by ultrashort laser pulses in subablation conditions, *Phys. Rev. B* **86**, 115316 (2012).
- [16] Y. Wang, L. Guo, X. Xu, J. Pierce, and R. Venkatasubramanian, Origin of coherent phonons in  $\text{Bi}_2\text{Te}_3$  excited by ultrafast laser pulses, *Phys. Rev. B* **88**, 064307 (2013).
- [17] A. R  mer, O. Osmani, and B. Rethfeld, Laser damage in silicon: Energy absorption, relaxation, and transport, *J. Appl. Phys.* **116**, 053508 (2014).
- [18] T. Shin, S. W. Teitelbaum, J. Wolfson, M. Kandyla, and K. A. Nelson, Extended two-temperature model for ultrafast thermal response of band gap materials upon impulsive optical excitation, *J. Chem. Phys.* **143**, 194705 (2015).
- [19] E. Petrakakis, G. D. Tsibidis, and E. Stratakis, Modelling of the ultrafast dynamics and surface plasmon properties of silicon upon irradiation with mid-IR femtosecond laser pulses, *Phys. Rev. B* **99**, 195201 (2019).
- [20] M. Segovia and X. Xu, High accuracy ultrafast spatiotemporal pump-probe measurement of electrical thermal transport in thin film gold, *Nano Lett.* **21**, 7228 (2021).
- [21] J. F. Young and H. M. van Driel, Ambipolar diffusion of high-density electrons and holes in Ge, Si, and GaAs: Many-body effects, *Phys. Rev. B* **26**, 2147 (1982).
- [22] Y. Shinohara, K. Yabana, Y. Kawashita, J. I. Iwata, T. Otobe, and G. F. Bertsch, Coherent phonon generation in time-dependent density functional theory, *Phys. Rev. B* **82**, 155110 (2010).
- [23] L. E. Black and D. H. Macdonald, On the quantification of Auger recombination in crystalline silicon, *Sol. Energy Mater. Sol. Cells* **234**, 111428 (2022).
- [24] M. Gu, Y. H. Bai, G. P. Zhang, M. El Mliles, Y. El Kouari, and A. Hajjaji, *Ab initio* study of electron and phonon coupling in silicon, *IOP Conf. Ser. Mater. Sci. Eng.* **948**, 012005 (2020).
- [25] D. E. Aspnes and A. A. Studna, Dielectric functions and optical parameters of Si, Ge, GaP, GaAs, GaSb, InP, InAs, and InSb from 1.5 to 6.0 eV, *Phys. Rev. B* **27**, 985 (1983).
- [26] D. Sangalli, S. Dal Conte, C. Manzoni, G. Cerullo, and A. Marini, Nonequilibrium optical properties in semiconductors from first principles: A combined theoretical and experimental study of bulk silicon, *Phys. Rev. B* **93**, 195205 (2016).
- [27] L. Tian, L. Di Mario, A. K. Sivan, D. Catone, P. O’Keeffe, A. Paladini, S. Turchini, and F. Martelli, Carrier dynamics in silicon nanowires studied via femtosecond transient optical spectroscopy from 1.1 to 3.5 eV, *Nanotechnology* **30**, 214001 (2019).
- [28] H. Vaghasiya, S. Krause, and P. T. Miclea, Thermal and non-thermal ablation mechanisms in crystalline silicon by femtosecond laser pulses: Classical approach of the carrier density two temperature model, *J. Phys. D: Appl. Phys.* **55**, 175109 (2022).
- [29] X. Gu, S. Li, and H. Bao, Thermal conductivity of silicon at elevated temperature: Role of four-phonon scattering and electronic heat conduction, *Int. J. Heat Mass Transfer* **160**, 120165 (2020).
- [30] J. Zhou, H. D. Shin, K. Chen, B. Song, R. A. Duncan, Q. Xu, A. A. Maznev, K. A. Nelson, and G. Chen, Direct observation of large electron–phonon interaction effect on phonon heat transport, *Nat. Commun.* **11**, 6040 (2020).
- [31] T. Chlouba, F. Troj  nek, J. Laube, D. Hiller, S. Gutsch, M. Zacharias, and P. Mal  y, Interplay of bimolecular and Auger recombination in photoexcited carrier dynamics in silicon nanocrystal/silicon dioxide superlattices, *Sci. Rep.* **8**, 1703 (2018).
- [32] M. I. Kaganov, I. M. Lifshitz, and L. V. Tanatarov, Relaxation between electrons and the crystalline lattice, *J. Exptl. Theoret. Phys. (U.S.S.R.)* **31**, 232 (1956) [*Sov. Phys. JETP* **4**, 173 (1957)].
- [33] S. I. Anisimov and B. Rethfeld, On the theory of ultrashort laser pulse interaction with a metal, in *Nonresonant Laser-Matter Interaction (NLMI-9)*, edited by V. I. Konov and M. N. Libenson, Vol. 3093 (International Society for Optics and Photonics, Bellingham, WA, 1997), pp. 192–203.
- [34] K. Sokolowski-Tinten and D. von der Linde, Generation of dense electron-hole plasmas in silicon, *Phys. Rev. B* **61**, 2643 (2000).
- [35] A. J. Sabbah and D. M. Riffe, Femtosecond pump-probe reflectivity study of silicon carrier dynamics, *Phys. Rev. B* **66**, 165217 (2002).
- [36] R. Biswas and V. Ambegaokar, Phonon spectrum of a model of electronically excited silicon, *Phys. Rev. B* **26**, 1980 (1982).
- [37] M. Schultze *et al.*, Attosecond band-gap dynamics in silicon, *Science* **346**, 1348 (2014).
- [38] S. Roth *et al.*, Photocarrier-induced band-gap renormalization and ultrafast charge dynamics in black phosphorus, *2D Mater.* **6**, 031001 (2019).
- [39] L. Meckbach, J. Hader, U. Huttner, J. Neuhaus, J. T. Steiner, T. Stroucken, J. V. Moloney, and S. W. Koch, Ultrafast band-gap renormalization and build-up of optical gain in monolayer  $\text{MoTe}_2$ , *Phys. Rev. B* **101**, 075401 (2020).
- [40] X. Y. Wang, D. M. Riffe, Y. S. Lee, and M. C. Downer, Time-resolved electron-temperature measurement in a highly excited gold target using femtosecond thermionic emission, *Phys. Rev. B* **50**, 8016 (1994).
- [41] B. E. Sernelius, Intraband relaxation time in highly excited semiconductors, *Phys. Rev. B* **43**, 7136 (1991).
- [42] E. Hendry, M. Koeberg, J. Pijpers, and M. Bonn, Reduction of carrier mobility in semiconductors caused by charge-charge interactions, *Phys. Rev. B* **75**, 233202 (2007).
- [43] M. Combescot and R. Combescot, Conductivity relaxation time due to electron-hole collisions in optically excited semiconductors, *Phys. Rev. B* **35**, 7986 (1987).
- [44] T. Terashige, H. Yada, Y. Matsui, T. Miyamoto, N. Kida, and H. Okamoto, Temperature and carrier-density dependence of electron-hole scattering in silicon investigated by optical-pump terahertz-probe spectroscopy, *Phys. Rev. B* **91**, 241201 (2015).
- [45] M. Rosling, H. Bleicher, P. Jonsson, and E. Nordlander, The ambipolar diffusion coefficient in silicon: Dependence on excess-carrier concentration and temperature, *J. Appl. Phys.* **76**, 2855 (1998).
- [46] A. L. Efros, Anomalous Low Temperature Ambipolar Diffusion and Einstein Relation, *Phys. Rev. Lett.* **104**, 116404 (2010).
- [47] A. Mouskeftaras, M. Chanal, M. Chambonneau, R. Clady, O. Ut  za, and D. Grojo, Direct measurement of ambipolar diffusion in bulk silicon by ultrafast infrared imaging of laser-induced microplasmas, *Appl. Phys. Lett.* **108**, 041107 (2016).
- [48] D. Macdonald and A. Cuevas, Validity of simplified Shockley-Read-Hall statistics for modeling carrier lifetimes in crystalline silicon, *Phys. Rev. B* **67**, 075203 (2003).

- [49] J. Kanasaki, H. Tanimura, K. Tanimura, P. Ries, W. Heckel, K. Biedermann, and T. Fauster, Ultrafast dynamics in photoexcited valence-band states of Si studied by time- and angle-resolved photoemission spectroscopy of bulk direct transitions, *Phys. Rev. B* **97**, 035201 (2018).
- [50] J. K. Chen, W. P. Latham, and J. E. Beraun, The role of electron–phonon coupling in ultrafast laser heating, *J. Laser Appl.* **17**, 63 (2005).
- [51] M. Hase, M. Katsuragawa, A. M. Constantinescu, and H. Petek, Frequency comb generation at terahertz frequencies by coherent phonon excitation in silicon, *Nat. Photonics* **6**, 243 (2012).
- [52] M. Bernardi, D. Vigil-Fowler, J. Lischner, J. B. Neaton, and S. G. Louie, *Ab Initio* Study of Hot Carriers in the First Picosecond after Sunlight Absorption in Silicon, *Phys. Rev. Lett.* **112**, 257402 (2014).